Geotechnical Engineering in the XXI Century: Lessons learned and future challenges
N.P. López-Acosta et al. (Eds.)

doi:10.3233/STAL190315

Experimental Study on the Two-Phase Fluid Flow in Porous Media During Repetitive Drainage-Imbibition Cycles Using Microfluidics Technique

Jingtao ZHANG[a], Haipeng ZHANG[b], Donghee LEE[c], Sangjin RYU[b] and Seunghee KIM[a,1]
[a]*Dept. of Civil Eng., Univ. of Nebraska-Lincoln, USA*
[b]*Dept. of Mech. & Materials Eng., Univ. of Nebraska-Lincoln, USA*
[c]*Dept. of Genetics, Univ. of Nebraska Medical Center, USA*

Abstract. Existing compressed air energy storage (CAES) facilities use salt dome caverns to store compressed air. On the other hand, other geologic formations, such as hard rock caverns, depleted gas reservoirs, and saline aquifers, are good alternatives. Storage of compressed air in either depleted gas reservoirs or saline aquifers involves two-phase fluid flow in porous media. That is, injection of non-wetting air into saturated porous media initiates a drainage process (i.e., non-wetting fluid displaces presiding wetting fluid), and the withdrawal of compressed air back to the surface to regenerate energy triggers an imbibition process (i.e., wetting fluid reoccupies the pore space). Moreover, the CAES operation is expected to run on a daily cycle, which means the drainage-imbibition process is likely to repeat a huge number of times. In this regard, a thorough understanding of the two-phase fluid flow during the cyclic injection and withdrawal of compressed air is critical to predict the performance of CAES in porous media and to improve its efficiency. In this study, the two-phase fluid flows during repetitive drainage-imbibition cycles are investigated using the microfluidics technique and polydimethylsiloxane (PDMS)-based models. Two different geometries, one with circular solids (Type I) and the other with square solids (Type II), which mimic unconsolidated rock sediment and a fracture network of carbonate rock, were prepared for the study. After a total of ten repetitive drainage-imbibition cycles, it was observed that the occupation efficiency of compressed air for Type I model converged to a certain value at different attempts. In contrast, the occupation efficiency of compressed air for Type II model yielded a pronounced fluctuation, which is partly due to the low residual saturation of non-wetting fluid before the next turn of drainage. Besides, prevalent displacement modes of wetting and non-wetting fluids at the pore-scale were noticeably different for the two-pore structures, which is manifested in the unpredictable pattern of non-wetting fluid flow for Type II over the extended cycles. In conclusion, the geometry of porous media has a great influence on the efficiency of repetitive drainage-imbibition cycles of two-phase fluid flow in porous media, and thus more elaborate study is needed to gain the confidence on the cyclic efficiency of CAES in porous media.

Keywords. Compressed air energy storage (CAES), fluid flow in porous media, repetitive drainage-imbibition cycles, microfluidics technology and PDMS model.

[1] Corresponding Author, Dept. of Civil Eng., Univ. of Nebraska-Lincoln, PKI 204D, 1110 S. 67th St, Omaha, NE, USA, email: seunghee.kim@unl.edu.

1. Introduction

Mounting concerns on the carbon emission have been driving many countries to explore more renewable energy production. Also, the inevitable intermittency of renewable energy necessitates a variety of viable energy storage systems (ESSs) to address the mismatch between energy demand and supply. Compressed air energy storage (CAES) is one of the ESSs, which has a low environmental impact and long lifespan [1]. The basic concept of CAES is that ambient air is compressed and stored in a subsurface storage medium using an electric compressor to convert excess off-peak electricity to mechanical energy. When the energy demand is high later, the compressed air is released back to drive a turbine generator to produce electricity (Figure 1).

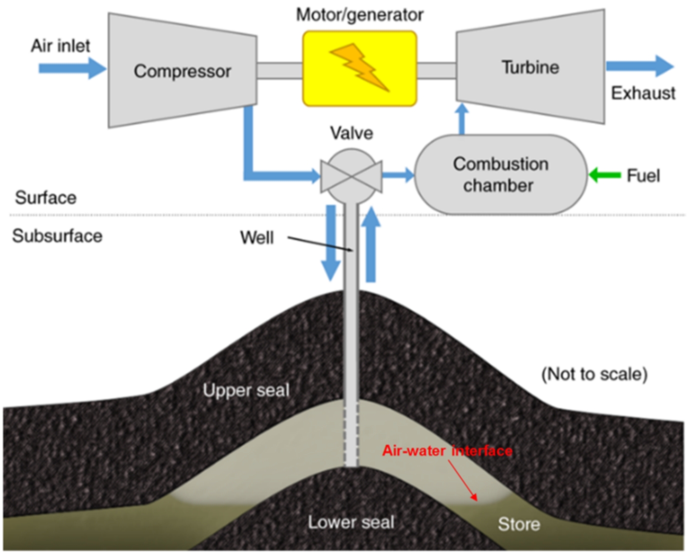

Figure 1. The schematic illustration of compressed air energy storage (CAES) in porous aquifer. The image is modified from Castillo et al., 2019 [2].

Cavern reservoirs and porous rock reservoirs can be utilized for the underground CAES. Compared to cavern reservoirs, porous rock reservoirs are distributed much more widely, and they can provide far higher storage capacity [3]. When the compressed air is injected into a porous rock reservoir, it involves immiscible two-phase fluid flow. In detail, injection of the non-wetting air into saturated porous aquifer initiates a drainage process, and the withdrawal of the compressed air triggers an imbibition process. Because the CAES operation is expected to run on a daily or seasonal basis, the drainage-imbibition process is likely to be repeated for numerous times. Therefore, a thorough understanding of the two-phase fluid flow during the repeated injection-and-withdrawal of compressed air under desired air injection/extraction rates is critical to predict and improve the performance of CAES. To date, there is no experimental study that delves into the repetitive two-phase fluid flow in porous media in relevance to either CAES operation or other energy/environmental operations. In this regard, we performed a pore-scale experimental study to elucidate the process of repetitive drainage-imbibition cycles in porous media using microfluidics technology.

2. Microfluidic study and governing numbers

2.1. PDMS (polydimethylsiloxane)-Based pore-Network micromodel

Because of the low cost, easiness to design, controllable surface wettability and the transparency for observation, either homogenous or heterogeneous PDMS-based micromodels have been widely used to simulate the porous structure of geologic materials. Compared to hard materials, a PDMS-based pore-network device is more flexible to modify and easier to fabricate [4].

2.2. Parameters and governing numbers

The two-phase fluid flow in porous media is heavily influenced by the capillary pressure P_c, capillary number Ca, viscosity number M and bond number Bo [5,6]:

$$P_c = \frac{2\gamma cos\theta}{r}, \;\; Ca = \frac{\mathrm{V} \cdot \mu_{nw}}{\gamma cos\theta}, \;\; M = \frac{\mu_{nw}}{\mu_w} \;\; and \;\; Bo = \frac{\Delta\rho g k}{\gamma} \tag{1}$$

where γ is the interfacial surface tension coefficient [mN/m], θ is the contact angle of a solid-fluid-fluid system [deg], r is the radius of a fluid flow channel, V is the velocity of an advancing non-wetting fluid [m/s], μ_{nw} is the viscosity of non-wetting fluid [Pa·s], μ_w is the viscosity of wetting fluid [Pa·s], $\Delta\rho$ is the density difference between the two fluid phases [kg/m^3], g is the gravitational acceleration [m/s^2], and k is the intrinsic permeability a hosting porous medium [m^2].

3. Experimental study

3.1. Fabrication of the pore-Network micromodel

First, the geometry of the micromodel was prepared using AutoCAD (Figure 2a). Then a transparent photomask was prepared based on the design (Figure 2b), which was used to produce a master mold using photolithography. The mold consisted of the positive relief of SU-8 100 photoresist (MicroChem) on a silicon wafer (Figure 2c). PDMS was prepared, poured over the mold and cured in an oven at 65˚C for 6 hours. The cured PDMS channel was then peeled away from the mold and bonded to a glass slide (spin-coated with a thin layer of cured PDMS in advance) via plasma activation (Figure 2d). Then, the fabricated device was cured in the oven at 65˚C for one day.

3.2. Geometry of micromodel

Type I consists of circular solids in the main domain to mimic unconsolidated (or partially consolidated) rock sediments, and Type II with square solids to emulate naturally fractured carbonate rocks. Note that the scale of both Type I and II models is rather pore-scale, so there is an inherent discrepancy between this pore-scale geometry and the fracture system at the field scale. The dimension of the main domain is 20 mm × 20 mm, and there are 48 × 50 solids for both Type I and II models. The height of the flow channel in both types was 100 μm. The inner diameter of pore space in Type I was

206 μm, and the pore space width in Type II was 80 μm (D_2 and B_2 in Figure 3, respectively). For comparison, the aperture of hydraulic paths in the rock and the width of fractures are generally in the range of $1\text{-}10^3$ μm [7]. Type I and II can be classified as retaining large and small aspect ratio, respectively [8]. The intrinsic permeability was measured to be 3,300 md for Type I and 4,300 md for Type II. Because the discrepancy in the permeability was insignificant, the porosity and permeability condition can be regarded as almost identical for Type I and II.

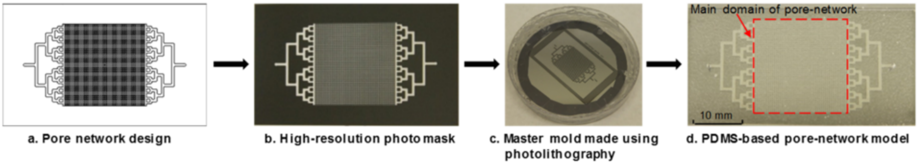

Figure 2. Fabrication of the microfluidic pore-network model.

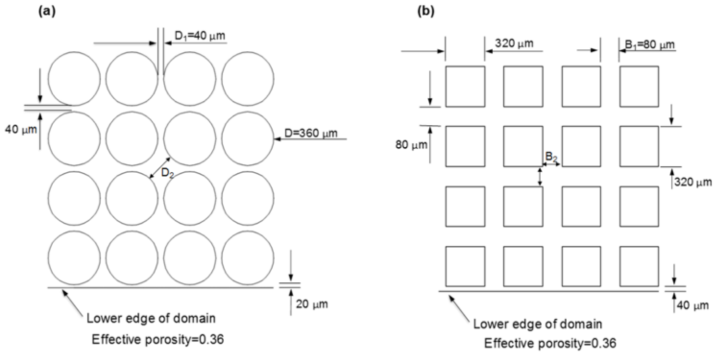

Figure 3. Geometry and dimension of the microfluidic pore-network model: (a) Type I and (b) Type II.

3.3. Materials

Mineral oil (Fisher Chemical BP2629-1) and water were selected as the wetting fluid ($\mu_w = 2.8\times10^{-2}$ Pa·s at 40°C, ρ_w = 830 kg/m^3 at 15°C) [9] and the non-wetting fluid (colored for visualization; $\mu_{nw} = 1.0\times10^{-3}$ Pa·s, ρ_{nw} = 1,000 kg/m^3), respectively, because PDMS is oleophilic. The surface tension coefficient between water and mineral oil is about 52 mN/m at 25°C [10]. The resultant *Ca* belongs to the lower end of *Ca* ranges from potential CAES projects. Also, the *M* value is similar to that for the air/water condition. Therefore, the condition of this study is relevant to the pore-scale air-water flow phenomena for an actual CAES project. The *Bo* is 1.1×10^{-7} (Type I) and 1.4×10^{-7} (Type II). Because $Bo \ll 1$, the gravity effect is deemed negligible.

3.4. Experimental setup and procedure

The micromodel was pre-saturated with the mineral oil (Figure 4). Two liquid containers (10 ml of mineral oil and 10 ml of water) were located at the same elevation. When the test was initiated, the water reservoir was lifted up to apply a head difference of 2 m, which caused the dyed water to invade into the micromodel (*i.e.*, drainage process; from right to the left-hand side of the model). The volumetric flow rate was measured to be around 0.005 ml/min for Type I and 0.015 ml/min for Type II during drainage, respectively. Accordingly, the drainage time was set at 7 min and 2.3 min to inject the water of 2.5 pore volumes of Type I and II, respectively. Once the drainage time reached the predetermined limit, the water reservoir was lowered down to its original height: completion of 1st drainage step. Next, the oil reservoir was elevated by 2 m to initiate the imbibition process. With that change, oil began to reoccupy the micromodel (i.e., imbibition: from left to the right-hand side). The volumetric flow rate was measured to be around 0.01 ml/min for Type I and 0.02 ml/min for Type II. Thus, the imbibition time was set as 3.5 min and 1.7 min for the oil of 2.5 pore volumes flows. Afterward, the oil reservoir was lowered back to its original height: completion of 1st imbibition step.

The above procedure was repeated to complete a total of ten cycles. These repetitive drainage-imbibition tests were conducted for a total of five different implementations with a micromodel newly fabricated each time for Type I and II.

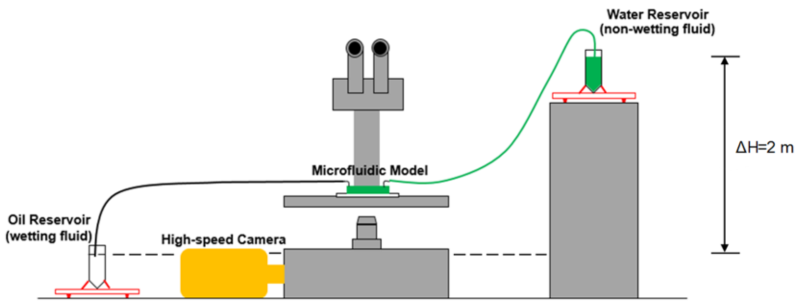

Figure 4. Experimental setup for applying repetitive drainage-imbibition cycles to the microfluidic device.

4. Experimental Results

Drainage and Imbibition. For Type I, displacement of oil by water at the end of the first drainage step appeared to resemble a viscous or capillary fingering, leaving behind considerable pore space unoccupied by water (Figure 5a-1st drainage). On the other hand, water invasion for Type II showed much more preferential developments in the horizontal direction (Figure 5b-1st drainage). Noticeably, the invasion of the non-wetting fluid for Type I stabilized to a certain pattern after first 2-3 drainage-imbibition cycles (Figure 5a). In contrast, water invasion was different at every cycle for Type II (Figure 5b). The amount of residual water was much greater in Type I than in Type II (Figure 6a). Similar to the drainage process, imbibition patterns were different for first 2-3 cycles but then stabilized as the drainage-imbibition cycle continued for Type I. In contrast, the imbibition pattern differed at every cycle for Type II (Figure 6b).

Sweep Efficiency and Effective Sweep Efficiency. Sweep efficiency, E_{nw}, is defined as the ratio of pore volume occupied by the non-wetting fluid to the entire pore volume in the micromodel after the drainage. The effective sweep efficiency, eE_{nw}, is defined as the ratio of pore volume occupied by non-wetting fluid after drainage to the pore volume occupied by wetting fluid before the drainage. The E_{nw} of Type I showed a convergence between 0.55 and 0.65 after a steeper fluctuation during first 2-3 injection cycles (Figure 7a). In contrast, the E_{nw} of Type II continued to display a pronounced fluctuation between 0.4 and 0.7 (Figure 7b). Note that, the average value of E_{nw} appears to be higher in Type I than Type II (i.e., 0.6 vs. 0.5). On the other hand, eE_{nw} of Type I (Figure 7c) continued to fluctuate during the cyclic injection between 0.1 and 0.4 after the first 2-3 cycles, which is lower than the overall E_{nw}. On the other hand, eE_{nw} of Type II (Figure 7d) fluctuated in the range of 0.3-0.5 during the later cycles of injection-withdrawal.

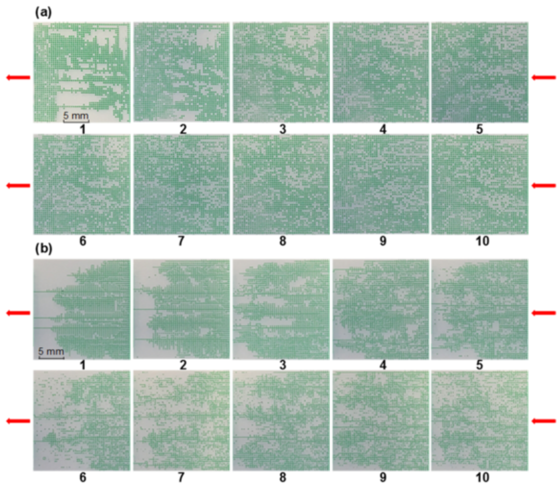

Figure 5. Distribution of water (colored) at the end of each drainage step (test #4): (a) Type I and (b) Type II.

Residual Saturation and Effective Residual Saturation. Residual saturation, S_{rnw}, is defined as the ratio of pore volume occupied by the non-wetting fluid to the entire pore volume in the micromodel, after the imbibition step. The effective residual saturation, eS_{rnw}, is expressed as the ratio of pore volume still occupied by non-wetting fluid after imbibition to the pore volume of non-wetting fluid before the imbibition. S_{rnw} shows a much larger amount of remaining water in Type I compared to that in Type II (mean ~0.4 vs. ~0.15; Figure 8a and b). Analysis of eS_{rnw} supports that more water was recessed back when oil imbibed for Type II (Figure 8c and d).

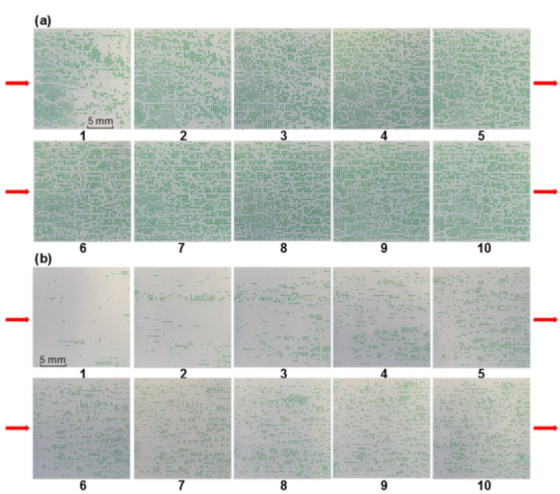

Figure 6. Distribution of oil (colorless) at the end of each imbibition step (test #4): (a) Type I and (b) Type II.

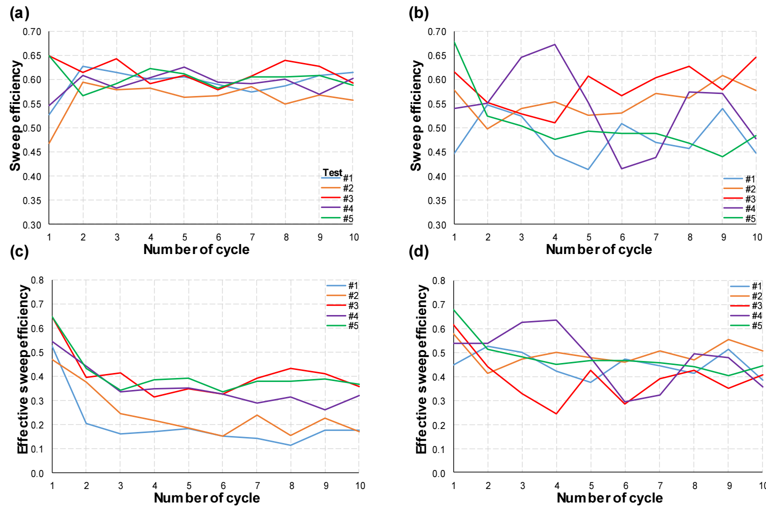

Figure 7. Sweep efficiency: (a) Type I, (b) Type II; and effective sweep efficiency: (c) Type I and (d) Type II.

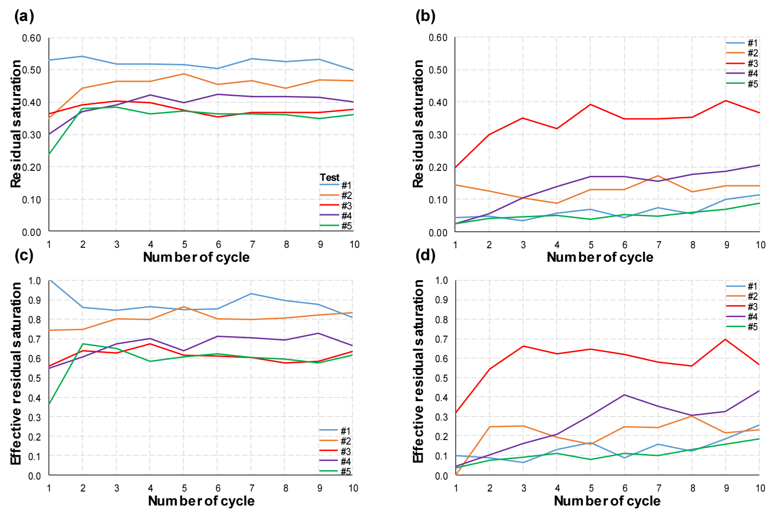

Figure 8. Residual saturation: (a) Type I, (b) Type II; and effective residual saturation: (c) Type I and (d) Type II.

5. Conclusion

Water injection in Type I appeared to resemble a viscous or capillary fingering, with a considerable occurrence of transverse propagation. The water invasion stabilized to a certain pattern after experiencing 2-to-3 drainage-imbibition cycles. On the other hand, a stable displacement pattern was rather observed near the inlet, and then it was localized towards the outlet during the first drainage step in Type II. Further, its pattern differed at every cycle, showing no evidence of flow pattern stabilization. During imbibition, a larger volume of water was displaced back in Type II than Type I. Imbibition patterns were again stabilized after the first 2-to-3 cycles in Type I, whereas it differed at every cycle in Type II.

The overall sweep efficiency of Type I showed a convergence between 0.55 and 0.65, while the overall sweep efficiency of Type II continually fluctuated between 0.4 and 0.7. On the other hand, the effective sweep efficiency continued to fluctuate during the cyclic injection within the range between 0.1 and 0.4, after the first 2-to-3 cycles, in Type I. And the effective sweep efficiency of Type II varied in the range between 0.3 and 0.5. The residual saturation showed that much higher volume of water was left behind in Type I after each imbibition step. Analysis of effective sweep efficiency and effective residual saturation suggests that the geometry of Type II helps to accommodate more non-wetting fluid during drainage and discharge it back more during imbibition.

Overall, it can be argued that under similar porosity and permeability conditions, rock formations that retain a Type II-like geometry can be utilized better for the purpose of repetitive air injection and withdrawal for the CAES application.

Acknowledgment

This research was supported by the Research Council: Interdisciplinary Grant at University of Nebraska-Lincoln (Grant No. 26-1107-9001-014) for S. Kim and S. Ryu, the Start-up Grant for S. Kim at University of Nebraska-Lincoln, and American Chemical Society Petroleum Research Fund for S. Ryu. We appreciate Stephen Morin for his assist in microfluidics master mold fabrication.

References

[1] A. Rogers, A. Henderson, X. Wang, and M. Negnevitsky, Compressed air energy storage: Thermodynamic and economic review. *IEEE Power and Energy Society General Meeting*, Maryland, USA, 2014.

[2] J. Mouli-Castillo, M. Wilkinson, D. Mignard, C. McDermott, R.S. Haszeldine, and Z.K. Shipton, Inter-seasonal compressed-air energy storage using saline aquifers, *Nature Energy* **4** (2019), 131–139.

[3] B. Wang and S. Bauer, Compressed air energy storage in porous formations: a feasibility and deliverability study, *Petroleum Geoscience* **23(3)** (2017), 206–314.

[4] S.K. Tang and G.M. Whitesides, Basic microfluidic and soft lithographic techniques. In: Y. Fainman, D. Psaltis and C. Yang (eds) *Optofluidics: Fundamentals, Devices, and Applications*, McGraw-Hill, New York, 2010.

[5] R. Lenormand, E. Touboul, and C. Zarcone, Numerical models and experiments on immiscible displacements in porous media, *Journal of Fluid Mechanics* **189** (1988), 165–87.

[6] S. Kim, D.N. Espinoza, J. Jung, M. Cha, and J.C. Santamarina, Carbon Geological Storage: Coupled Processes, Engineering and Monitoring. In: P. Newell and A. llgen (eds) *Science of Carbon Storage in Deep Saline Formations: Process Coupling Across Time and Spatial Scales*, Elsevier, Amsterdam, 2018.

[7] N. E. Odling, Permeability of natural and simulated fracture patterns. In: R.M. Larsen, H. Brekke, B.T. Larsen and E. Talleraas (eds) *Structural and Tectonic Modelling and its Application to Petroleum Geology*, Elsevier, Amsterdam, 1992.

[8] R. Lenormand, Liquids in porous media, *Journal of Physics: Condensed Matter* **2(S)** (1990), SA79–88.

[9] Lakeland University. https://lakeland.edu/PDFs/MSDS/1117/Mineral Oil (Fisher).pdf.

[10] S.M.S. Murshed, S.H. Tan, and N.T. Nguyen, Temperature dependence of interfacial properties and viscosity of nanofluids for droplet-based microfluidics, *Journal of Physics D: Applied Physics* **41(8)** (2008), 085502.